Journal of Applied Analysis and Computation
Volume 16, Number 5, October 2026, 2515–2539
Website:http://www.jaac-online.com
DOI:10.11948/20260026

A PERIODICITY DEGREE FOR TIME-T MAPS: DETECTION AND A POSTERIORI CERTIFICATION OF PERIODIC ORBITS

Wanjia Gong[1,†]

Abstract We develop a scalar interface between numerical detection and a posteriori certification of T-periodic solutions in time-periodic ODEs. Starting from the time-T map, we introduce the *periodicity degree*, a bounded indicator of one-period recurrence, and establish its basic analytical properties on compact sets. The periodicity degree serves as an optimization-friendly detector of near-fixed points of the time-T map. To convert such numerical evidence into a mathematically valid existence statement, we provide a contraction-based a posteriori criterion that upgrades a detected near-fixed point to the existence of an exact fixed point with an explicit error bound. Numerical illustrations for two forced benchmarks clarify the distinction between detection and certification, while a Lorenz double-scroll example shows how recurrence-guided lag selection and local Poincaré/Newton refinement can be combined to obtain and interpret a high-accuracy periodic-orbit candidate in a chaotic regime.

Keywords Periodic orbits, near recurrence, a posteriori validation, Poincaré map, Lorenz system.

MSC(2010) 34C25, 37C27.

1. Introduction

Periodic solutions are fundamental objects in the qualitative and quantitative analysis of nonlinear dynamical systems. For time-periodic forcing, a T-periodic orbit represents a recurrent regime synchronized with the external period, and it provides a natural reference for stability, bifurcation, and response analysis [11]. From a computational viewpoint, periodic orbits are typically characterized as fixed points of the time-T (Poincaré) map, and numerical continuation methods track such solutions under parameter variation; this philosophy underlies a substantial body of algorithmic and software development in bifurcation analysis [7]. Beyond forced systems, periodic orbits also play a structural role in chaotic dynamics: Unstable periodic orbits form a dense and dynamically organizing skeleton, supporting periodic-orbit expansions and symbolic descriptions [1,2,5,10,20].

Two practical difficulties recur across these settings. First, *detection* of periodicity from data or black-box simulations is inherently delicate: One typically observes near-returns rather than exact closure, especially along long transients or on chaotic attractors. Recurrence-based diagnostics, originating with recurrence plots and their quantitative variants, provide a standard way to visualize and score such near recurrences along trajectories [8,16,21,22]. More recently, recurrence information has also been encoded in network form via *directed recurrence networks*, whose structural and spectral properties have been used to analyze nonlinear and complex dynamical

[†]The corresponding author.
[1]College of Mathematics, Jilin University, Changchun 130012, China
Email: gongwj22@mails.jlu.edu.cn(W. Gong)

systems [6]. Recent recurrence-guided and data-driven approaches have also been developed for extracting recurrent motions and periodic-orbit candidates from complex simulations [9,17]. Second, even when a numerical procedure produces a candidate with small residual, converting this numerical evidence into a mathematically valid existence statement requires an *a posteriori certification* step. The gap between detection and certification is particularly pronounced in sensitive systems (e.g. the Lorenz flow [15]), where near-returns can be intermittent and where discretization and rounding effects may mask the underlying logical implications.

Rigorous and validated numerics provide one principled route from numerical evidence to proof. A prototypical example is Tucker's computer-assisted proof of a strange attractor for the Lorenz equations [19]. More generally, contraction-based a posteriori frameworks—such as the radii polynomial approach and its Fourier/automatic-differentiation realizations—have become effective tools for certifying periodic orbits and related invariant objects [12,13]. These ideas also support validated continuation along branches of periodic solutions in suitable functional settings [3]. However, in many applications one still lacks a lightweight *scalar* indicator that (i) is easy to evaluate from a computed time-T map, (ii) can be optimized or scanned over large sets to localize candidates, and (iii) interfaces cleanly with a posteriori certification without conflating numerical evidence with exact periodicity.

This paper develops such an interface for T-periodic ordinary differential equations. Our starting point is the one-period mismatch of the time-T map on a prescribed compact set Ω. We introduce a bounded scalar function $x_0 \mapsto \rho(x_0)$, called the periodicity degree function, which quantifies one-period recurrence at a point and yields set-level summaries through extremization over Ω. Because the pointwise function ρ is a monotone transform of the one-period displacement, maximizing the periodicity degree is equivalent to minimizing the one-period mismatch. This makes it a convenient detector of near-fixed points of the time-T map. We then provide a complementary *certification* step: A contraction-mapping a posteriori criterion which upgrades a detected near-fixed point into a guarantee that an exact fixed point exists nearby, and hence that an exact T-periodic solution exists.

The resulting framework is illustrated on two T-periodic benchmarks and on the Lorenz double-scroll regime. In the Lorenz study, we emphasize a reproducible workflow: A lag-based recurrence scan identifies candidate return-time scales along a chaotic trajectory, and a subsequent Poincaré/Newton refinement produces a high-accuracy periodic-orbit candidate. Its interpretation is then clarified by phase-dependent recurrence envelopes and by the certification interface. This viewpoint aligns with the established role of unstable periodic orbits in the Lorenz attractor and its symbolic/periodic-orbit descriptions [5,20].

The paper is organized as follows. Section 2 defines the periodicity degree and establishes its basic analytical properties. Section 3 formulates the a posteriori certification theorem and gives checkable sufficient conditions in terms of residual and local contraction bounds. Section 4 presents benchmark illustrations, separating detection from certification in practice, and Section 5 demonstrates how recurrence-driven detection and local refinement interface in a chaotic setting.

2. Periodicity degree

In this section, we consider a T-periodic system and introduce a scalar function that quantifies one-period recurrence through the associated time-T map. We study the initial value problem

$$\dot{x} = f(t, x), \qquad x(0) = x_0, \tag{2.1}$$

where $f : \mathbb{R} \times \mathbb{R}^n \to \mathbb{R}^n$ is T-periodic in time, i.e.,

$$f(t+T,x) = f(t,x), \qquad \forall\, (t,x) \in \mathbb{R} \times \mathbb{R}^n.$$

To guarantee existence and uniqueness of Carathéodory solutions on $[0,T]$ and to ensure continuous dependence on initial data, we impose the following standard hypotheses.

Assumption 2.1. (H1) Carathéodory regularity. *For every $x \in \mathbb{R}^n$, the map $t \mapsto f(t,x)$ is measurable; and for almost every $t \in [0,T]$, the map $x \mapsto f(t,x)$ is continuous.*

(H2) Local x-Lipschitz with an L^1 bound. *For every $R > 0$, there exists a function $L_R \in L^1(0,T)$ such that for all $t \in [0,T]$ and all $x, y \in \mathbb{R}^n$ with $|x| \le R$ and $|y| \le R$,*

$$|f(t,x) - f(t,y)| \le L_R(t)\,|x-y|.$$

(H3) Integrable linear growth bound. *There exist functions $a, b \in L^1(0,T)$ such that for all $t \in [0,T]$ and all $x \in \mathbb{R}^n$,*

$$|f(t,x)| \le a(t) + b(t)\,|x|.$$

Let $\Omega \subset \mathbb{R}^n$ be a nonempty compact set. Under **(H1)**–**(H3)**, for each $x_0 \in \Omega$ there exists a unique Carathéodory solution $x(\cdot, x_0)$ of (2.1) on $[0,T]$, see [4] and [18]. This defines the time-T map

$$\Phi_T : \Omega \to \mathbb{R}^n, \qquad \Phi_T(x_0) := x(T, x_0). \tag{2.2}$$

Continuous dependence on initial conditions implies that Φ_T is continuous on Ω.

We next define a measure of one-period recurrence on Ω by comparing $\Phi_T(x_0)$ with x_0.

Periodicity degree function. For $x_0 \in \Omega$, let

$$r(x_0) := \big|\Phi_T(x_0) - x_0\big| \tag{2.3}$$

denote the one-period displacement. Define $\rho : \Omega \to \mathbb{R}$ by

$$\rho(x_0) = \begin{cases} \dfrac{\log\big(1 + r(x_0)\big)}{r(x_0)}, & r(x_0) > 0, \\ 1, & r(x_0) = 0. \end{cases} \tag{2.4}$$

This normalization gives a continuous extension at $r(x_0) = 0$ and assigns the maximal value $\rho(x_0) = 1$ precisely at fixed points of Φ_T. Geometrically, $r(x_0) = \|\Phi_T(x_0) - x_0\|$ measures the one-period mismatch of the trajectory issued from x_0, namely the distance between the initial state and its image under the time-T map. Accordingly, $\rho(x_0)$ can be interpreted as a normalized one-period recurrence score, with values close to 1 indicating strong one-period recurrence. The logarithmic normalization keeps the score in $(0,1]$ while compressing large mismatches.

We aggregate the recurrence information over Ω by taking the infimum of ρ on Ω.

Definition 2.1 (Periodicity degree on Ω)**.** Assume **(H1)**–**(H3)** and let Φ_T be given by (2.2). The *periodicity degree of system* (2.1) *on* Ω is defined as

$$\rho(\Omega) := \inf_{x_0 \in \Omega} \rho(x_0). \tag{2.5}$$

Since Ω is compact, it is important that the infimum in (2.5) is attained.

Theorem 2.1. *Let $\Omega \subset \mathbb{R}^n$ be a nonempty compact set and consider the T-periodic system* (2.1). *Assume* **(H1)**–**(H3)** *and define Φ_T by* (2.2) *and ρ by* (2.4). *Then there exists $x^* \in \Omega$ such that*

$$\rho(x^*) = \inf_{x_0 \in \Omega} \rho(x_0) = \rho(\Omega).$$

In particular, the periodicity degree $\rho(\Omega)$ is attained.

Proof. Since Φ_T is continuous on Ω, the map $x_0 \mapsto \Phi_T(x_0) - x_0$ is continuous, hence $r(x_0) = |\Phi_T(x_0) - x_0|$ is continuous on Ω. The auxiliary function

$$g(r) = \begin{cases} \dfrac{\log(1+r)}{r}, & r > 0, \\ 1, & r = 0, \end{cases}$$

is continuous on $[0, \infty)$, so $\rho(x_0) = g(r(x_0))$ is continuous on Ω. By compactness of Ω, ρ attains its minimum on Ω, and the minimizer x^* satisfies $\rho(x^*) = \inf_{x_0 \in \Omega} \rho(x_0) = \rho(\Omega)$. □

We next connect the extremal value $\rho = 1$ to fixed points of Φ_T and hence to genuine T-periodic solutions.

Theorem 2.2. *Assume* **(H1)**–**(H3)**. *Let $\Omega \subset \mathbb{R}^n$ be nonempty and compact, and let Φ_T and ρ be defined as above. Then for every $x_0 \in \Omega$ the following are equivalent:*

$$\rho(x_0) = 1 \quad \Longleftrightarrow \quad \Phi_T(x_0) = x_0 \quad \Longleftrightarrow \quad x(t+T, x_0) = x(t, x_0) \text{ for all } t \in [0, T].$$

Consequently, $\rho(x_0) = 1$ if and only if the solution issued from x_0 extends to a T-periodic solution on $\mathbb{R}$; in particular,

$$x(t + kT, x_0) = x(t, x_0), \qquad \forall\, t \in [0, T],\ \forall\, k \in \mathbb{N}.$$

Proof. If $\Phi_T(x_0) = x_0$, then $r(x_0) = 0$ and thus $\rho(x_0) = 1$ by (2.4). Conversely, if $\rho(x_0) = 1$ and $r(x_0) > 0$, then $\log(1 + r(x_0)) = r(x_0)$, which is impossible since $\log(1+r) < r$ for all $r > 0$. Hence $r(x_0) = 0$, so $\Phi_T(x_0) = x_0$. This proves $\rho(x_0) = 1 \iff \Phi_T(x_0) = x_0$.

If $x(t + T, x_0) = x(t, x_0)$ for all $t \in [0, T]$, then $x(T, x_0) = x(0, x_0) = x_0$, hence $\Phi_T(x_0) = x_0$. Conversely, assume $\Phi_T(x_0) = x_0$ and define $h(t) := x(t+T, x_0)$ on $[0, T]$. Using the T-periodicity of f and the Carathéodory property,

$$\dot{h}(t) = f(t + T, x(t + T, x_0)) = f(t, h(t)) \quad \text{a.e. on } [0, T], \qquad h(0) = x(T, x_0) = x_0.$$

Thus $h(\cdot)$ and $x(\cdot, x_0)$ solve the same IVP on $[0, T]$; uniqueness under **(H1)**–**(H2)** gives $h(t) = x(t, x_0)$ for all $t \in [0, T]$, i.e. $x(t + T, x_0) = x(t, x_0)$ on $[0, T]$. Iteration yields T-periodicity on $\mathbb{R}$. □

The preceding theorem leads to a compactness-based criterion for periodic solutions in Ω.

Corollary 2.1. *Under the assumptions of Theorem 2.2, the following statements are equivalent:*

(a) The system (2.1) *admits a T-periodic solution with initial value in Ω.*

(b) $\max_{x_0 \in \Omega} \rho(x_0) = 1$.

Proof. Since Ω is compact and ρ is continuous on Ω, ρ attains its maximum on Ω. If (a) holds, then there exists $x_0 \in \Omega$ such that $\Phi_T(x_0) = x_0$, hence $\rho(x_0) = 1$ by Theorem 2.2, which implies

(b). Conversely, if (b) holds, then there exists $\bar{x}_0 \in \Omega$ with $\rho(\bar{x}_0) = 1$, hence $\Phi_T(\bar{x}_0) = \bar{x}_0$ and (a) follows. □

The quantities above compare $x(T, x_0)$ to x_0 at the initial phase $t = 0$. To capture recurrence variability along a trajectory, we now allow comparison at arbitrary phases $t \in \mathbb{R}$. This requires global-in-time well-posedness; accordingly, we work under the following time-global hypotheses.

Assumption 2.2. *In addition to* **(H1)**, *we replace* **(H2)**–**(H3)** *by the following time-global versions.*

(H2$^\sharp$) Local x-Lipschitz with a local L^1 bound on $\mathbb{R}$. *For every $R > 0$, there exists a function $\Lambda_R \in L^1_{\mathrm{loc}}(\mathbb{R})$ such that for a.e. $t \in \mathbb{R}$ and all $x, y \in \mathbb{R}^n$ with $|x| \le R$ and $|y| \le R$,*

$$|f(t, x) - f(t, y)| \le \Lambda_R(t)\,|x - y|.$$

(H3$^\sharp$) Integrable linear growth bound on $\mathbb{R}$. *There exist functions $\alpha, \beta \in L^1_{\mathrm{loc}}(\mathbb{R})$ such that for a.e. $t \in \mathbb{R}$ and all $x \in \mathbb{R}^n$,*

$$|f(t, x)| \le \alpha(t) + \beta(t)\,|x|.$$

We now define the one-period mismatch at phase t along the orbit and the associated envelope quantities.

Definition 2.2 (Maximal/minimal periodicity degree along a trajectory)**.** Assume **(H1)** and Assumption 2.2. Fix $x_0 \in \Omega$ and let $x(\cdot, x_0)$ denote the corresponding solution. For each $t \in \mathbb{R}$ define the one-period displacement along the orbit by

$$\kappa(t, x_0) := \big|x(t + T, x_0) - x(t, x_0)\big|. \tag{2.6}$$

Define the associated pointwise periodicity degree along the orbit by

$$\rho\big(x(t, x_0)\big) := \begin{cases} \dfrac{\log\big(1 + \kappa(t, x_0)\big)}{\kappa(t, x_0)}, & \kappa(t, x_0) \neq 0, \\ 1, & \kappa(t, x_0) = 0. \end{cases} \tag{2.7}$$

The *maximal* and *minimal* periodicity degrees along the trajectory are

$$\overline{\rho}(x_0) := \sup_{t \in \mathbb{R}} \rho\big(x(t, x_0)\big), \tag{2.8}$$

and

$$\underline{\rho}(x_0) := \inf_{t \in \mathbb{R}} \rho\big(x(t, x_0)\big). \tag{2.9}$$

For a finite horizon $L > 0$, define

$$\overline{\rho}_{[0,L]}(x_0) := \sup_{t \in [0,L]} \rho\big(x(t, x_0)\big), \qquad \underline{\rho}_{[0,L]}(x_0) := \inf_{t \in [0,L]} \rho\big(x(t, x_0)\big). \tag{2.10}$$

For a fixed initial value $x_0 \in \Omega$, the quantity $\overline{\rho}(x_0)$ describes the strongest one-period recurrence occurring along the entire orbit, while $\underline{\rho}(x_0)$ describes the weakest one-period recurrence. Hence the interval $\big[\underline{\rho}(x_0), \overline{\rho}(x_0)\big]$ provides a trajectory-wise envelope of one-period recurrence strengths.

We first verify that these envelope quantities are well-defined under the global hypotheses.

Theorem 2.3. *Let $\Omega \subset \mathbb{R}^n$ be nonempty and compact, and consider the T-periodic system (2.1). Assume* **(H1)** *and Assumption 2.2. Then for every $x_0 \in \Omega$ the quantities $\overline{\rho}(x_0)$ and $\underline{\rho}(x_0)$ defined in (2.8)–(2.9) are well-defined and satisfy*

$$0 \le \underline{\rho}(x_0) \le \overline{\rho}(x_0) \le 1.$$

Moreover, there exist sequences $\{t_j^+\}_{j\in\mathbb{N}}$ and $\{t_j^-\}_{j\in\mathbb{N}}$ in $\mathbb{R}$ such that

$$\rho\big(x(t_j^+, x_0)\big) \to \overline{\rho}(x_0), \qquad \rho\big(x(t_j^-, x_0)\big) \to \underline{\rho}(x_0) \quad \text{as } j \to \infty.$$

Proof. Fix $x_0 \in \Omega$. Under **(H1)** and Assumption 2.2, there is a unique maximal Carathéodory solution $x(\cdot, x_0)$ on an interval $(t_-(x_0), t_+(x_0))$ containing 0. We claim that $t_-(x_0) = -\infty$ and $t_+(x_0) = +\infty$.

Set $u(t) := |x(t, x_0)|$. By **(H3$^\sharp$)** and $|\dot{x}| = |f(t, x)|$ a.e., we have for a.e. t,

$$u'(t) \le \alpha(t) + \beta(t)\, u(t).$$

Fix any finite $S \in (0, t_+(x_0))$. Grönwall's inequality on $[0, S]$ yields, for all $t \in [0, S]$,

$$u(t) \le \Big(u(0) + \int_0^t \alpha(s) \exp\Big(-\int_0^s \beta(\tau)\, d\tau\Big)\, ds\Big) \times \exp\Big(\int_0^t \beta(\tau)\, d\tau\Big).$$

Since $\alpha, \beta \in L^1_{\mathrm{loc}}(\mathbb{R})$, the right-hand side is finite on every finite interval, hence we have $\sup_{t\in[0,S]} |x(t, x_0)| < \infty$. Therefore no finite-time blow-up can occur forward in time, and $t_+(x_0) = +\infty$. The same argument applied to $t \mapsto x(-t, x_0)$ gives $t_-(x_0) = -\infty$. Consequently, $x(t, x_0)$ is defined for all $t \in \mathbb{R}$, so (2.6)–(2.7) are well-defined for all $t \in \mathbb{R}$.

By construction, $\rho(x(t, x_0)) \in (0, 1]$ for all $t \in \mathbb{R}$, hence the set $\{\rho(x(t, x_0)) : t \in \mathbb{R}\} \subset (0, 1]$ is nonempty and bounded. Therefore $\overline{\rho}(x_0)$ and $\underline{\rho}(x_0)$ exist and satisfy $0 \le \underline{\rho}(x_0) \le \overline{\rho}(x_0) \le 1$.

Finally, the defining properties of supremum and infimum give sequences $\{t_j^+\}$ and $\{t_j^-\}$ with $\rho(x(t_j^+, x_0)) \to \overline{\rho}(x_0)$ and $\rho(x(t_j^-, x_0)) \to \underline{\rho}(x_0)$. □

Remark 2.1. Assume **(H1)**–**(H2$^\sharp$)** so that solutions are locally well-posed and unique. Suppose in addition that Ω is a compact *invariant* set for (2.1), i.e. for every $x_0 \in \Omega$ the corresponding solution exists for all $t \in \mathbb{R}$ and satisfies $x(t, x_0) \in \Omega$ for all $t \in \mathbb{R}$. Then $\overline{\rho}(x_0)$ and $\underline{\rho}(x_0)$ in Definition 2.2 are automatically well-defined for every $x_0 \in \Omega$.

Corollary 2.2. *Under the assumptions of Theorem 2.3, fix $x_0 \in \Omega$. If $\overline{\rho}(x_0) = \underline{\rho}(x_0) = 1$, then the corresponding solution is T-periodic, i.e.,*

$$x(t + T, x_0) = x(t, x_0), \qquad \forall\, t \in \mathbb{R}.$$

Proof. By definition,

$$\underline{\rho}(x_0) \le \rho\big(x(t, x_0)\big) \le \overline{\rho}(x_0), \qquad \forall\, t \in \mathbb{R}.$$

If $\overline{\rho}(x_0) = \underline{\rho}(x_0) = 1$, then $\rho(x(t, x_0)) \equiv 1$ on $\mathbb{R}$, hence $\kappa(t, x_0) = 0$ for all $t \in \mathbb{R}$ by (2.7), which is exactly T-periodicity. □

Fix $x_0 \in \Omega$ and $L > 0$. Since $t \mapsto x(t, x_0)$ is continuous and the map in (2.7) is continuous in κ, the function $t \mapsto \rho(x(t, x_0))$ is continuous on $[0, L]$. Hence $\overline{\rho}_{[0,L]}(x_0)$ and $\underline{\rho}_{[0,L]}(x_0)$ in (2.10) are attained on $[0, L]$. Moreover, if $\underline{\rho}_{[0,L]}(x_0) = 1$, then $\kappa(t, x_0) = 0$ for all $t \in [0, L]$, and in particular the solution issued from x_0 is T-periodic.

3. A posteriori certification and its interface with the periodicity degree

Section 2 established a clean *logical* characterization: By Theorem 2.2 and Corollary 2.1, the existence of a T-periodic solution with initial value in Ω is equivalent to $\max_{x_0\in\Omega}\rho(x_0)=1$. In computations, however, one typically observes $\rho(\widehat{x})\approx 1$ at some numerically determined candidate $\widehat{x}\in\Omega$. Since ρ is a monotone transform of the one-period mismatch r in (2.3)–(2.4), this numerical observation should be interpreted as *small mismatch* $r(\widehat{x})\ll 1$, but it does not by itself yield the exact identity $\Phi_T(\widehat{x})=\widehat{x}$. The purpose of this section is to provide a *rigorous a posteriori criterion* that upgrades a *detected* near-fixed point into a mathematically valid statement that an *exact* fixed point exists nearby, and hence an exact T-periodic solution exists. The a posteriori criterion stated below can be viewed as a Newton–Kantorovich-type validation result for the fixed-point equation $\Phi_T(x)=x$ via a quasi-Newton operator. Our contribution is not the contraction principle itself, but its explicit formulation in terms of computable residual and local contraction bounds, together with its clean interface with the periodicity-degree detector introduced in Section 2.

Recall that $r(x_0)=|\Phi_T(x_0)-x_0|$ and $\rho(x_0)=\varphi(r(x_0))$ with φ strictly decreasing and $\varphi(0)=1$. Thus maximizing ρ over Ω is an optimization-friendly *detector* of near zeros of the displacement map

$$d(x):=\Phi_T(x)-x,\qquad \text{s.t.}\qquad r(x)=|d(x)|.$$

Certification, by contrast, is a local analysis step: Starting from a candidate $\widehat{x}$ with small residual $r(\widehat{x})$, one verifies conditions that guarantee the existence of a true zero x^* of d in a neighborhood of $\widehat{x}$. Once such an x^* is obtained, Theorem 2.2 immediately yields a T-periodic solution.

For the certification step we impose an additional smoothness assumption: We assume that the time-T map is continuously differentiable on a neighborhood of the candidate point. Throughout, $|\cdot|$ denotes the norm used in (2.3), and $\|\cdot\|$ denotes the corresponding induced operator norm.

Theorem 3.1. *Let $\Omega\subset\mathbb{R}^n$ be closed, let $\widehat{x}\in\Omega$, and define $d(x)=\Phi_T(x)-x$. Assume that $d\in C^1$ on a neighborhood of the closed ball $B_R(\widehat{x})\subset\Omega$. Let $A\in\mathbb{R}^{n\times n}$ be invertible and define the Newton-type map*

$$\mathcal{N}(x):=x-A\,d(x)=x-A\big(\Phi_T(x)-x\big).$$

Suppose that there exist $R>0$ and $q\in[0,1)$ such that

$$\eta:=|\mathcal{N}(\widehat{x})-\widehat{x}|=|A\,d(\widehat{x})|\le(1-q)R, \tag{3.1}$$

$$\sup_{x\in B_R(\widehat{x})}\|D\mathcal{N}(x)\|=\sup_{x\in B_R(\widehat{x})}\|I-A\,Dd(x)\|\le q<1. \tag{3.2}$$

Then $\mathcal{N}$ maps $B_R(\widehat{x})$ into itself and is a contraction on $B_R(\widehat{x})$. Consequently, there exists a unique $x^*\in B_R(\widehat{x})$ such that

$$x^*=\mathcal{N}(x^*)\quad\Longleftrightarrow\quad d(x^*)=0\quad\Longleftrightarrow\quad\Phi_T(x^*)=x^*.$$

In particular, the system admits a T-periodic solution with initial value $x^*\in\Omega$, and

$$|x^*-\widehat{x}|\le R. \tag{3.3}$$

Proof. Fix $x \in B_R(\widehat{x})$. By the triangle inequality,

$$|\mathcal{N}(x) - \widehat{x}| \le |\mathcal{N}(x) - \mathcal{N}(\widehat{x})| + |\mathcal{N}(\widehat{x}) - \widehat{x}|.$$

Since $\mathcal{N} \in C^1$ on $B_R(\widehat{x})$, the mean value inequality yields

$$|\mathcal{N}(x) - \mathcal{N}(\widehat{x})| \le \Big(\sup_{z \in B_R(\widehat{x})} \|D\mathcal{N}(z)\| \Big) |x - \widehat{x}| \le q\, R,$$

where we used (3.2) and $|x - \widehat{x}| \le R$. Using (3.1), we have

$$|\mathcal{N}(x) - \widehat{x}| \le qR + (1-q)R = R,$$

so $\mathcal{N}(x) \in B_R(\widehat{x})$. Hence $\mathcal{N}$ maps the ball into itself.

For $x, y \in B_R(\widehat{x})$, the same argument gives

$$|\mathcal{N}(x) - \mathcal{N}(y)| \le \Big(\sup_{z \in B_R(\widehat{x})} \|D\mathcal{N}(z)\| \Big) |x - y| \le q\, |x - y|,$$

so $\mathcal{N}$ is a contraction on the complete metric space $B_R(\widehat{x})$. By Banach's fixed-point theorem, there exists a unique $x^* \in B_R(\widehat{x})$ such that $x^* = \mathcal{N}(x^*)$. Since A is invertible, this implies $d(x^*) = 0$, i.e. $\Phi_T(x^*) = x^*$. Finally, (3.3) holds because $x^* \in B_R(\widehat{x})$. □

Because ρ is strictly decreasing in $r(x) = |d(x)|$, a maximizer of ρ on Ω yields a point where $|d(x)|$ is small. Theorem 3.1 shows that smallness of $|d(\widehat{x})|$ becomes an existence statement once it is complemented by a verified *local contraction bound* for $\mathcal{N}$. When the theorem applies, it produces an exact fixed point x^*, together with a quantitative a posteriori error bound (3.3).

Condition (3.2) involves a supremum over $B_R(\widehat{x})$. A standard way to make it explicit is to bound the variation of Dd on $B_R(\widehat{x})$ by a Lipschitz constant. Since $d(x) = \Phi_T(x) - x$, this reduces to bounding the variation of $D\Phi_T$.

Assume, in addition, that there exists a compact set $U \subset \mathbb{R}^n$ such that $x(t, x_0) \in U$ for all $t \in [0, T]$ and all $x_0 \in B_R(\widehat{x})$, and that f is continuous in t and twice continuously differentiable in x on $[0, T] \times U$. For x_0 in that ball, denote by $x(t, x_0)$ the solution and by $X(t, x_0) = D\Phi_t(x_0)$ the variational flow, which satisfies

$$\dot{X}(t) = D_x f\big(t, x(t, x_0)\big)\, X(t), \qquad X(0) = I. \tag{3.4}$$

Then $D\Phi_T(x_0) = X(T, x_0)$ and

$$Dd(x_0) = D\Phi_T(x_0) - I. \tag{3.5}$$

Define

$$K_1 := \sup_{t \in [0,T],\, x \in U} \|D_x f(t, x)\|, \qquad K_2 := \sup_{t \in [0,T],\, x \in U} \|D_x^2 f(t, x)\|.$$

Lemma 3.1. *Under the above assumptions, for all $x, y \in B_R(\widehat{x})$ one has*

$$\|D\Phi_T(x) - D\Phi_T(y)\| \le L_\Phi\, |x - y|, \qquad L_\Phi := \begin{cases} K_2\, e^{K_1 T} \dfrac{e^{K_1 T} - 1}{K_1}, & K_1 > 0, \\ K_2\, T, & K_1 = 0. \end{cases} \tag{3.6}$$

Consequently, $\|Dd(x) - Dd(y)\| \le L_\Phi\, |x - y|$ on $B_R(\widehat{x})$.

Proof. Let $x(t) = x(t, x_0)$ and $y(t) = x(t, y_0)$. Since $\|D_x f\| \le K_1$ on $[0,T] \times U$, Grönwall's inequality yields $|x(t) - y(t)| \le e^{K_1 t}|x_0 - y_0|$ for $t \in [0,T]$. Let $X(t)$ and $Y(t)$ solve (3.4) along $x(t)$ and $y(t)$, respectively. Subtracting the variational equations gives

$$\frac{d}{dt}(X - Y) = D_x f(t, x(t))(X - Y) + \big(D_x f(t, x(t)) - D_x f(t, y(t))\big)Y.$$

Taking norms and using $\|Y(t)\| \le e^{K_1 t}$ (again by Grönwall) and the Lipschitz bound $\|D_x f(t,\xi) - D_x f(t,\eta)\| \le K_2|\xi - \eta|$ on U, we obtain

$$\frac{d}{dt}\|X - Y\| \le K_1\|X - Y\| + K_2\,|x(t) - y(t)|\,e^{K_1 t} \le K_1\|X - Y\| + K_2\,e^{2K_1 t}|x_0 - y_0|.$$

With $\|X(0) - Y(0)\| = 0$, Grönwall yields

$$\|X(T) - Y(T)\| \le K_2 e^{K_1 T}\Big(\int_0^T e^{K_1 s}\,ds\Big)\,|x_0 - y_0| = K_2 e^{K_1 T}\frac{e^{K_1 T} - 1}{K_1}\,|x_0 - y_0|,$$

with the obvious modification when $K_1 = 0$. Since $D\Phi_T(x_0) = X(T)$ and $D\Phi_T(y_0) = Y(T)$, (3.6) follows. The statement for Dd follows from (3.5). □

Lemma 3.1 yields a convenient sufficient condition for (3.2). Indeed, if we choose

$$A := (Dd(\widehat{x}))^{-1} = \big(D\Phi_T(\widehat{x}) - I\big)^{-1},$$

then $I - A\,Dd(\widehat{x}) = 0$ and for any $x \in B_R(\widehat{x})$,

$$\|I - A\,Dd(x)\| = \|A(Dd(\widehat{x}) - Dd(x))\| \le \|A\|\,L_\Phi\,|x - \widehat{x}| \le \|A\|\,L_\Phi\,R.$$

Hence (3.2) holds with

$$q := \|A\|\,L_\Phi\,R \qquad \text{provided} \qquad q < 1, \tag{3.7}$$

and (3.1) becomes the explicit residual requirement

$$\|A\|\,r(\widehat{x}) = \|A\|\,|d(\widehat{x})| \le (1 - q)R. \tag{3.8}$$

Taken together, (3.7)–(3.8) give a fully checkable a posteriori criterion.

Remark 3.1. The detect–refine–validate workflow described above is not restricted to situations in which the time-T map Φ_T has a unique fixed point in Ω. If several T-periodic orbits coexist, then the landscape of the periodicity degree function $x \mapsto \rho(x)$ may exhibit several local maxima, or more generally several disjoint high-recurrence regions, corresponding to different periodic-orbit candidates. In that case, the detection step can be carried out globally over Ω, while the a posteriori certification theorem can be applied separately in neighborhoods of the refined candidates. Thus, the detection stage is global, whereas the certification stage is local and can be performed orbit by orbit.

Remark 3.2. The conditions (3.7)–(3.8) are *sufficient* for the existence of a fixed point of Φ_T in $B_R(\widehat{x})$. Failure to verify them does not imply nonexistence of T-periodic solutions; it only indicates that the present choice of $\widehat{x}$, A, R, or the available bounds is not strong enough to certify a contraction on the prescribed neighborhood.

Remark 3.3. The implications of Theorem 3.1 are logically unconditional; in applications, however, the status of the conclusion depends on whether the quantities entering (3.7)–(3.8) are obtained as *validated* bounds or merely as floating-point approximations. Validated enclosures (e.g. interval integration for Φ_T and $D\Phi_T$, and interval linear algebra for $\|A\|$) turn the inequalities into a computer-assisted proof, whereas non-validated computations should be read as high-confidence numerical evidence.

In particular, whenever (3.7)–(3.8) can be verified for some candidate $\widehat{x}$, Theorem 3.1 yields an exact fixed point x^* of Φ_T satisfying $|x^* - \widehat{x}| \le R$. In the next section, we apply this certification principle to the concrete systems considered later and discuss how the required bounds can be obtained in practice.

4. Numerical illustrations of the periodicity degree

In this section we present two T-periodic benchmark systems to illustrate the results of Section 2 and to clarify the dynamical meaning of the periodicity degree. Our goal is to show how the spatial indicator $\rho(x_0)$ and the trajectory-wise envelopes $\overline{\rho}_{[0,L]}(x_0)$ and $\underline{\rho}_{[0,L]}(x_0)$ behave in practice.

Let $\Omega \subset \mathbb{R}^n$ be the compact set specified in each benchmark and let T be the forcing period. For each $x_0 \in \Omega$ we approximate the time-T map by numerical integration on $[0, T]$ and denote

$$\widehat{\Phi}_T(x_0) \approx \Phi_T(x_0).$$

Unless stated otherwise, we use an adaptive explicit Runge–Kutta method with dense output, relative tolerance 10^{-10} and absolute tolerance 10^{-12}.

The one-period mismatch is evaluated by the numerical residual associated with (2.3),

$$\widehat{r}(x_0) := \big\|\widehat{\Phi}_T(x_0) - x_0\big\|,$$

and the pointwise periodicity degree is computed by applying the same scalar transform as in (2.4) to $\widehat{r}(x_0)$. In implementations, $\log(1+\widehat{r})$ is evaluated using `log1p` to avoid loss of significance for very small residuals. Since the transform in (2.4) is strictly decreasing for positive arguments, near-maximizers of ρ correspond to near-minimizers of the residual and are natural candidates for the fixed-point equation $\Phi_T(x) = x$.

To approximate extremal values of ρ on Ω in the planar benchmarks, we sample Ω on a uniform Cartesian grid and evaluate $\widehat{r}$ at each grid point. The best and worst grid points are then refined by a bound-constrained local search on Ω, carried out on the smooth surrogate $J(x) := \frac{1}{2}\,\widehat{r}(x)^2$. The local solver is treated as derivative-free, and bound constraints are enforced by projection onto Ω.

For trajectory-wise quantities on a finite horizon $[0, L]$, we use the orbit mismatch $\kappa(t, x_0)$ in (2.6) and the associated pointwise indicator in (2.7). Numerically, for a fixed x_0 we integrate on $[0, L+T]$ and sample times $t_i = i\Delta t$ on $[0, L]$ with $\Delta t = T/M$. Using dense output, we evaluate

$$\widehat{\kappa}(t_i, x_0) := \big\|\widehat{x}(t_i + T, x_0) - \widehat{x}(t_i, x_0)\big\|$$

and apply the same scalar transform as in (2.7). The finite-horizon envelopes $\overline{\rho}_{[0,L]}(x_0)$ and $\underline{\rho}_{[0,L]}(x_0)$ from Definition 2.2 are approximated by the corresponding discrete extrema over the sampled times.

4.1. Benchmark I: Forced damped linear oscillator

We first revisit the forced damped oscillator

$$\begin{cases} \dot{q} = p, \\ \dot{p} = -2\zeta\, p - \omega_0^2 q + F\cos(\omega t), \end{cases} \qquad (q,p) \in \mathbb{R}^2, \tag{4.1}$$

which is T-periodic in time with $T = 2\pi/\omega$. The vector field is smooth in (t, x) and globally Lipschitz in x with at most linear growth, hence the standing assumptions **(H1)**–**(H3)** hold.

Parameters, domain, and horizons. We fix

$$\omega = 1, \quad T = 2\pi, \quad \omega_0 = 1.6, \quad \zeta = 0.15, \quad F = 1.$$

This choice yields a clear transient toward the steady T-periodic regime: The damping produces rapid convergence, while the forcing remains strong enough to generate a nontrivial periodic response in the (q, p)-plane.

We take

$$\Omega := [-4, 4] \times [-4, 4] \subset \mathbb{R}^2,$$

evaluate the spatial periodicity degree $x_0 \mapsto \rho(x_0)$ on a uniform 201×201 grid on Ω, and refine the grid-based extremizers by a local search constrained to Ω. For the trajectory-wise periodicity envelopes, we use the horizon $L = 20T$ and sampling step $\Delta t = T/200$.

Writing $x = (q, p)^\top$ and $u(t) = (0, F\cos(\omega t))^\top$, (4.1) can be expressed as $\dot{x} = Ax + u(t)$ with

$$A = \begin{pmatrix} 0 & 1 \\ -\omega_0^2 & -2\zeta \end{pmatrix}.$$

The time-T map admits the affine representation

$$\Phi_T(x_0) = e^{AT}x_0 + \int_0^T e^{A(T-s)}u(s)\, ds =: e^{AT}x_0 + b_T,$$

and the one-period displacement field is therefore affine:

$$d(x_0) := \Phi_T(x_0) - x_0 = (e^{AT} - I)x_0 + b_T.$$

Since $\zeta > 0$ implies $\Re\lambda(A) < 0$, the Poincaré iteration $x_{k+1} = \Phi_T(x_k)$ is contractive in an equivalent norm. Consequently, Φ_T admits a unique fixed point $x^\sharp$, and every orbit converges to it.

Periodicity degree: Detection versus a posteriori certification. Figure 1(a) visualizes the pointwise periodicity degree $x_0 \mapsto \rho(x_0)$. Since $g(r) = \log(1 + r)/r$ is strictly decreasing for $r > 0$, maximizing ρ over Ω is equivalent to minimizing the one-period mismatch. Accordingly, the pronounced peak identifies a *detected* near-fixed point of the time-T map, denoted $\widehat{x}_{\max}$. Numerically, this detection is quantified by the residual

$$\widehat{r}(\widehat{x}_{\max}) = \|\widehat{\Phi}_T(\widehat{x}_{\max}) - \widehat{x}_{\max}\| \approx 3.90 \times 10^{-13},$$

so that $\rho(\widehat{x}_{\max}) = g(\widehat{r}(\widehat{x}_{\max}))$ is indistinguishable from 1 at plotting resolution.

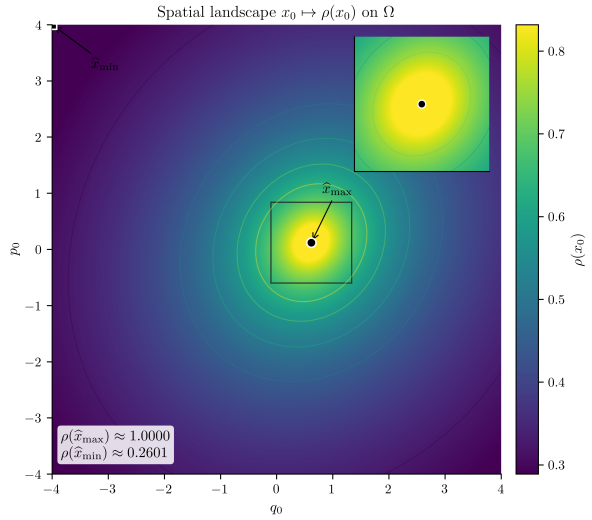

(a) Spatial periodicity degree $x_0 \mapsto \rho(x_0)$ on Ω (zoom near $\widehat{x}_{\max}$).

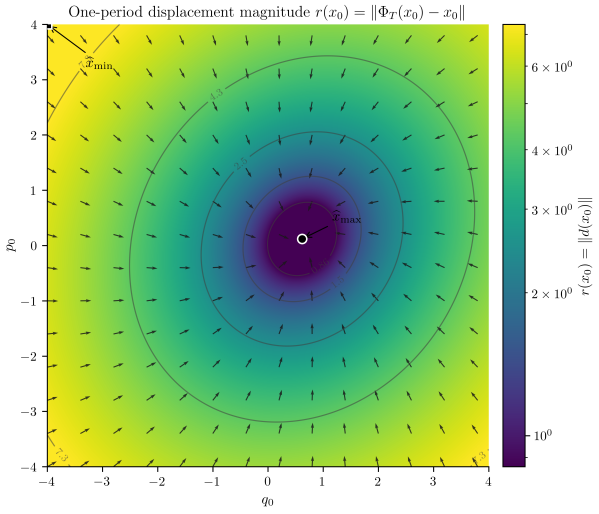

(b) One-period mismatch landscape $x_0 \mapsto \widehat{r}(x_0)$ with a sparse direction field.

Figure 1. Benchmark I. Filled markers indicate $\widehat{x}_{\max}$ (circle) and $\widehat{x}_{\min}$ (square).

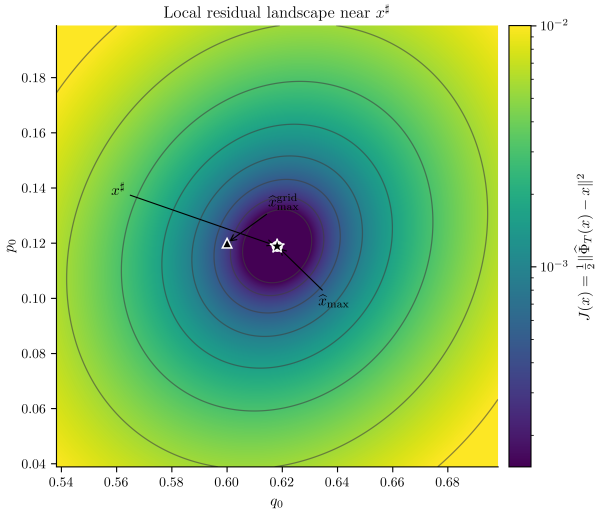

Figure 2. Benchmark I. Local landscape of $J(x) = \dfrac{1}{2}\|\widehat{\Phi}_T(x) - x\|^2$ in a neighborhood of $x^\sharp$; markers indicate $\widehat{x}^{\text{grid}}_{\max}$, $\widehat{x}_{\max}$, and $x^\sharp$.

However, the theoretical equivalence in Corollary 2.1 is *exact*: a T-periodic solution with initial value in Ω exists if and only if $\max_\Omega \rho = 1$, which requires an exact fixed point of the true map Φ_T. Therefore, $\rho(\widehat{x}_{\max}) \approx 1$ should be interpreted as a reliable *detector* of near recurrence, and it must be supplemented by an a posteriori certification step (Section 3) to produce a logically valid statement about an exact periodic orbit.

In Benchmark I, such a certification is particularly transparent because Φ_T is affine: the fixed-point equation $\Phi_T(x) = x$ reduces to the linear system

$$(I - e^{AT})x = b_T,$$

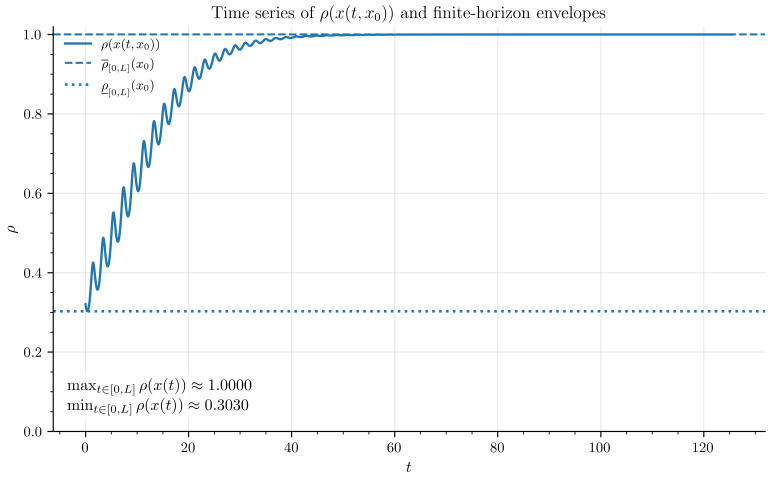

Figure 3. Time evolution of $\rho(x(t,x_0))$ on $[0,L]$ for a representative $x_0 \in \Omega$, together with the finite-horizon envelopes $\overline{\rho}_{[0,L]}(x_0)$ and $\underline{\rho}_{[0,L]}(x_0)$.

which can be solved directly. Let $x^\sharp$ denote this solution. In our computation,

$$\widehat{r}(x^\sharp) = \|\widehat{\Phi}_T(x^\sharp) - x^\sharp\| \approx 1.39 \times 10^{-17}, \qquad \|\widehat{x}_{\max} - x^\sharp\| \approx 3.03 \times 10^{-13}.$$

Figure 2 provides a geometric view of the same logic: The grid detector $\widehat{x}_{\max}^{\text{grid}}$ localizes the basin of the minimum of $J(x) = \frac{1}{2}\|\widehat{\Phi}_T(x) - x\|^2$, the derivative-free refinement produces $\widehat{x}_{\max}$ near the bottom of the valley, and the affine solve yields $x^\sharp$ at machine precision.

What $\rho(\Omega) = \inf_\Omega \rho$ measures in this benchmark. The periodicity degree on Ω, defined as $\rho(\Omega) = \inf_{x_0\in\Omega} \rho(x_0)$, describes the *worst* one-period recurrence over the chosen set. In Figure 1(a), the minimizer $\widehat{x}_{\min}$ occurs near the boundary of Ω and yields a substantially smaller value (about 2.6×10^{-1} in computation), reflecting that some initial conditions in Ω can have a relatively poor one-period return even though the dynamics converges to a globally attracting periodic response. Thus, $\rho(\Omega)$ should be read as a conservative, set-dependent robustness indicator, rather than as an existence test for periodic solutions.

Figure 3 illustrates the trajectory-wise meaning of the periodicity degree. Along a typical trajectory $x(t,x_0)$, the values $\rho(x(t,x_0))$ increase toward 1 as t grows, reflecting convergence toward the attracting T-periodic regime. The envelopes $\underline{\rho}_{[0,L]}(x_0)$ and $\overline{\rho}_{[0,L]}(x_0)$ quantify this transient variability: $\underline{\rho}_{[0,L]}(x_0)$ is attained during an early mismatch-dominated phase, whereas $\overline{\rho}_{[0,L]}(x_0)$ is attained after the orbit has nearly synchronized with the periodic response.

4.2. Benchmark II: Forced damped pendulum

We next consider a nonlinear T-periodic benchmark in which one-period recurrence is strongly phase-dependent. The model is the harmonically forced damped pendulum

$$\begin{cases} \dot{\theta} = \nu, \\ \dot{\nu} = -c\,\nu - \sin\theta + A\cos(\omega t), \end{cases} \qquad (\theta,\nu) \in \mathbb{R}^2, \tag{4.2}$$

whose vector field is T-periodic in time with $T = 2\pi/\omega$.

Standing hypotheses. The right-hand side in (4.2) is smooth in (t, θ, ν) and globally Lipschitz in (θ, ν), with at most linear growth; hence **(H1)**–**(H3)** hold and the time-T map Φ_T is continuous on any compact set.

Parameters, domain, and horizons. We fix

$$\omega = 1, \quad T = 2\pi, \quad c = 0.15, \quad A = 1.20, \tag{4.3}$$

and consider the compact set

$$\Omega := [-2\pi, 2\pi] \times [-4, 4] \subset \mathbb{R}^2,$$

sampled on a uniform 241×241 grid. For trajectory-wise envelopes we use $L = 40T$ and $\Delta t = T/200$.

Why $\rho \approx 1$ requires validation in this benchmark. In contrast to Benchmark I, the pendulum is naturally posed on the cylinder $\mathbb{S}^1 \times \mathbb{R}$, since θ is an angle modulo 2π. Consequently, a trajectory may satisfy

$$\theta(t+T) \approx \theta(t) + 2\pi m, \qquad \nu(t+T) \approx \nu(t),$$

for some integer m (phase-locked rotations), even when $\theta(t+T) \neq \theta(t)$ as real numbers. In such a situation, the Euclidean mismatch $r(x_0) = \|\Phi_T(x_0) - x_0\|$ is not the appropriate recurrence measure for detecting periodicity on the cylinder.

To align the numerical indicator with the geometry of (4.2), we therefore use the *cylindrical one-period mismatch*

$$r_{\mathrm{cyl}}(x_0) := \min_{m \in \mathbb{Z}} \big\| \Phi_T(x_0) - x_0 - (2\pi m, 0)^\top \big\|, \qquad x_0 = (\theta_0, \nu_0) \in \Omega, \tag{4.4}$$

and define the corresponding pointwise recurrence indicator by the *same* scalar transform

$$\rho_{\mathrm{cyl}}(x_0) := g\big(r_{\mathrm{cyl}}(x_0)\big), \qquad g(r) = \frac{\log(1+r)}{r} \ (r > 0), \ g(0) = 1.$$

By construction,

$$\rho_{\mathrm{cyl}}(x_0) = 1 \iff \exists\, m \in \mathbb{Z} : \ \Phi_T(x_0) = x_0 + (2\pi m, 0)^\top,$$

which is exactly the condition that the solution through x_0 is T-periodic on $\mathbb{S}^1 \times \mathbb{R}$ (with winding number m). Thus ρ_{cyl} plays the same role as ρ in Corollary 2.1, but now on the correct state space for the pendulum.

Figure 4(a) shows the spatial landscape $x_0 \mapsto \rho_{\mathrm{cyl}}(x_0)$ on Ω. As in Benchmark I, high values indicate strong one-period recurrence; however, the nonlinear geometry produces localized "islands" and "bands", reflecting pronounced phase dependence. In particular, the *periodicity degree on* Ω, namely

$$\rho_{\mathrm{cyl}}(\Omega) := \inf_{x_0 \in \Omega} \rho_{\mathrm{cyl}}(x_0),$$

quantifies the *worst* one-period recurrence across the domain: A small value means that Ω contains initial conditions whose one-period return is poor (large r_{cyl}), even if other parts of Ω contain highly recurrent states.

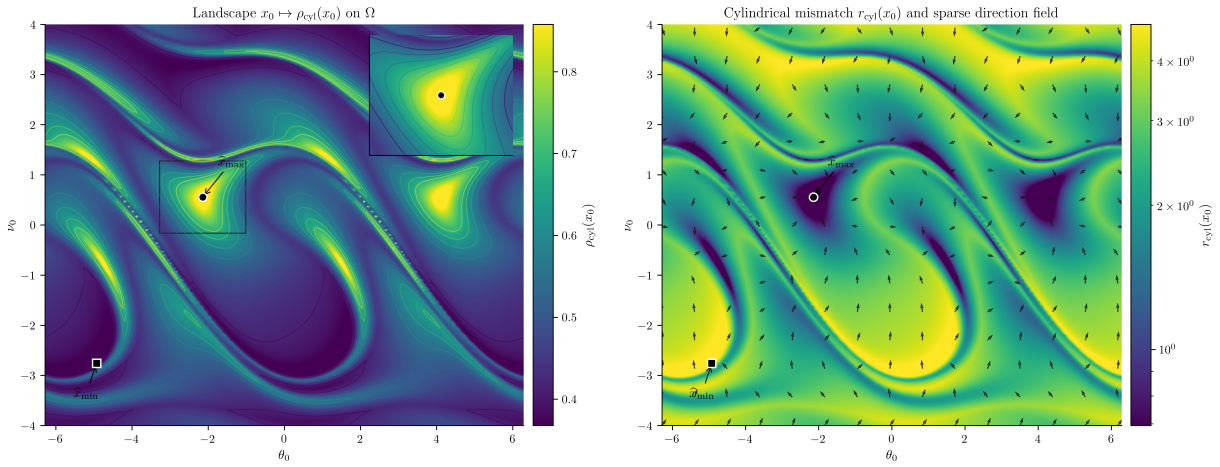

(a) Landscape $x_0 \mapsto \rho_{\mathrm{cyl}}(x_0)$ on Ω.

(b) Cylindrical mismatch $r_{\mathrm{cyl}}(x_0)$ and sparse direction field.

Figure 4. Benchmark II on the cylinder $\mathbb{S}^1 \times \mathbb{R}$. Markers indicate the refined maximizer $\widehat{x}_{\max}$ (filled circle) and minimizer $\widehat{x}_{\min}$ (filled square) of ρ_{cyl} on Ω.

The peak in Figure 4(a) should be interpreted as a *detection* of a candidate phase-locked periodic state. Denote the refined maximizer by $\widehat{x}_{\max}$ and let

$$\widehat{m} \in \arg\min_{m \in \mathbb{Z}} \left\| \Phi_T(\widehat{x}_{\max}) - \widehat{x}_{\max} - (2\pi m, 0)^\top \right\|.$$

A small mismatch $r_{\mathrm{cyl}}(\widehat{x}_{\max})$ is strong evidence but is not, by itself, a proof. To turn detection into a numerical verification, we perform an *a posteriori* shooting test on the lifted fixed-point equation

$$F_{\widehat{m}}(x) := \Phi_T(x) - x - (2\pi\widehat{m}, 0)^\top = 0. \tag{4.5}$$

A posteriori test. We compute the Jacobian

$$DF_{\widehat{m}}(x) = D\Phi_T(x) - I$$

by integrating the variational equation along the trajectory issued from x. Starting from $\widehat{x}_{\max}$, we apply one (or a few) Newton–shooting corrections

$$x^{(k+1)} = x^{(k)} - \left(DF_{\widehat{m}}(x^{(k)})\right)^{-1} F_{\widehat{m}}(x^{(k)}),$$

and certify the candidate whenever the residual $\|F_{\widehat{m}}(x^{(k)})\|$ is reduced to the level of the time-integration accuracy and the Jacobian remains well-conditioned. In the present parameter regime (4.3), the detected maximizer satisfies

$$r_{\mathrm{cyl}}(\widehat{x}_{\max}) \approx 6.9 \times 10^{-11}, \qquad \rho_{\mathrm{cyl}}(\widehat{x}_{\max}) \approx 1 - 3.4 \times 10^{-11},$$

and one Newton correction produces a high-accuracy numerical solution $x^\sharp$ of (4.5) with

$$\|F_{\widehat{m}}(x^\sharp)\| \approx 5.3 \times 10^{-13}, \qquad \rho_{\mathrm{cyl}}(x^\sharp) \approx 1 - 2.6 \times 10^{-13}.$$

Hence the "$\rho \approx 1$" feature in the landscape corresponds here to an actual T-periodic solution on $\mathbb{S}^1 \times \mathbb{R}$.

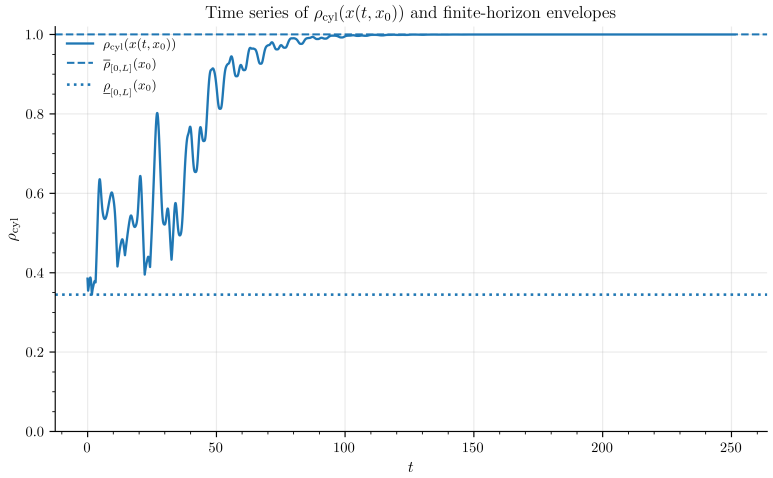

Figure 5. Benchmark II: Time evolution of $\rho_{\mathrm{cyl}}(x(t,x_0))$ on $[0,L]$ together with the finite-horizon envelopes $\overline{\rho}_{[0,L]}(x_0)$ and $\underline{\rho}_{[0,L]}(x_0)$.

Figure 4(b) visualizes the cylindrical mismatch $r_{\mathrm{cyl}}(x_0)$ and a sparse direction field for the lifted displacement $\Phi_T(x_0) - x_0 - (2\pi m^*(x_0), 0)^\top$, where $m^*(x_0)$ is the minimizer in (4.4). The arrows provide a geometric explanation of the recurrence landscape.

Finally, Figure 5 shows the time series $t \mapsto \rho_{\mathrm{cyl}}(x(t,x_0))$ together with the finite-horizon envelopes $\overline{\rho}_{[0,L]}(x_0)$ and $\underline{\rho}_{[0,L]}(x_0)$ (defined in Section 2 with κ computed using the same cylindrical convention as in (4.4)). The visible gap between these envelopes quantifies phase-dependent recurrence variability: The orbit experiences intermittent near-returns (peaks close to 1) as well as phases of poor one-period return.

5. Lorenz double-scroll: Periodicity degree on a chaotic attractor

We demonstrate the periodicity-degree framework of Section 2 and its certification interface of Section 3 on the classical Lorenz system in the chaotic double-scroll regime. Since the Lorenz vector field is autonomous, it is T-periodic in the sense of Section 2 for *every* $T > 0$. This example is particularly informative: The attractor contains infinitely many (typically unstable) periodic orbits [10], while a generic orbit is nonperiodic and exhibits only intermittent near recurrences.

We consider the Lorenz ODE

$$\dot{x} = \sigma(y - x), \qquad \dot{y} = x(\varrho - z) - y, \qquad \dot{z} = xy - \beta z, \tag{5.1}$$

at the standard chaotic parameters

$$\sigma = 10, \qquad \beta = \frac{8}{3}, \qquad \varrho = 28,$$

and we use the Euclidean norm $|\cdot| = \|\cdot\|_2$ throughout. In all computations below, the trajectory segment remains in the compact box

$$\Omega := [-20, 20] \times [-30, 30] \times [0, 55] \subset \mathbb{R}^3.$$

The standing hypotheses **(H1)**–**(H3)** hold for (5.1) on any finite interval $[0, T]$ because $f(t, x) \equiv F(x)$ is smooth; hence the time-T map Φ_T is well-defined and continuous on Ω.

Unless stated otherwise, trajectories are computed with an adaptive explicit Runge–Kutta method with dense output, relative tolerance 10^{-10} and absolute tolerance 10^{-12}.

5.1. Lag selection for the Lorenz data: A single-scan two-pass procedure

This subsection specifies, in a fully reproducible way, how the lag parameter T used in the Lorenz study is selected from data. Throughout, for each fixed lag T we write $\kappa(t)$ for the corresponding one-period mismatch signal along the trajectory. The goal of the present step is *detection*: To extract a short list of lags for which near-recurrences are statistically strong and reasonably consistent over time.

Windowed recurrence statistics. We compute a single long trajectory $x(t)$ on $[0, t_{\text{end}}]$ and discard a transient $[0, t_{\text{trans}}]$. To assess whether a given lag produces intermittent near-returns *repeatedly* (rather than in a single accidental episode), we evaluate statistics on J windows

$$I_j := [s_j,\, s_j + L], \qquad j = 1, \dots, J,$$

with $t_{\text{trans}} \le s_1 < \cdots < s_J$ and $s_J + L + p_{\max} T_{\max} \le t_{\text{end}}$, where $p_{\max}$ is the largest harmonic multiplier used (here $p_{\max} = 2$).

For each lag T and each window I_j, we summarize the depth of near-returns by a lower quantile

$$K_j(T) \;:=\; Q_\gamma\big(\{\kappa(t) : t \in I_j\}\big),$$

where Q_γ denotes the γ-quantile (we use $\gamma = 0.05$). Aggregating across windows yields a robust *score* and a window-to-window *spread*:

$$\mathcal{S}(T) \;:=\; \text{median}_{1 \le j \le J} K_j(T), \qquad \mathcal{D}(T) \;:=\; Q_{0.75}\big(\{K_j(T)\}\big) - Q_{0.25}\big(\{K_j(T)\}\big).$$

Small $\mathcal{S}(T)$ indicates that a majority of windows contain unusually small mismatch values, while $\mathcal{D}(T)$ measures how stable this behavior is across the windows.

In addition, we record window minima

$$m_j(T) := \min_{t \in I_j} \kappa(t),$$

and define a *hit-rate* at threshold $\varepsilon > 0$ by

$$h(T, \varepsilon) \;:=\; \frac{1}{J} \#\Big\{ j \in \{1, \dots, J\} :\; m_j(T) < \varepsilon \Big\}.$$

This is the fraction of windows in which at least one near-return crosses the absolute level ε.

All quantities above are evaluated on a uniform grid $T \in [T_{\min}, T_{\max}]$ with step ΔT. Crucially, the expensive part is performed only once: We compute $x(t)$ a single time and evaluate $x(t+T)$ via dense output, so the full scan over all T does not require repeated ODE integrations.

Pass–1: Significant valley detection on $\mathcal{S}(T)$. We evaluate the score $\mathcal{S}(T)$ on a uniform lag grid $\{T_k\}_{k=0}^{N} \subset [T_{\min}, T_{\max}]$ with spacing ΔT. To obtain a stable coarse candidate set, we smooth the discrete profile $k \mapsto \mathcal{S}(T_k)$ and detect *significant valleys* as local minima subject to: (i) A minimum separation (to avoid clusters of near-duplicate minima) and (ii) a prominence threshold (to reject shallow oscillations of the score landscape). The output of Pass–1 is an ordered valley list

$$\mathcal{V} := \{T^{(1)}, \dots, T^{(M)}\} \subset \{T_k\},$$

ranked by increasing smoothed score.

Pass–2: Consistency filtering and calibration of the hit threshold. On a chaotic attractor, small values of $\mathcal{S}(T)$ may be produced by highly localized episodes and can be strongly phase dependent. We therefore refine the Pass–1 valley list by imposing three deterministic consistency constraints:

$$\begin{aligned} &h(T,\varepsilon) \geq h_{\min}, \\ &\mathcal{D}(T) \leq \mathcal{D}_{\text{thr}}, \\ &\operatorname{perc}\big(\mathcal{S}(2T)\big) \leq \pi_{\max}, \qquad T \in \mathcal{V}, \end{aligned} \tag{5.2}$$

where $h(T,\varepsilon)$ is the window hit-rate, $\mathcal{D}(T)$ is the window-to-window spread, and $\operatorname{perc}(\mathcal{S}(2T))$ denotes the percentile rank of the harmonic score among the scanned grid values. Dynamically, these constraints enforce recurrence that is (i) *repeated in time* (hit-rate), (ii) not excessively *phase-sensitive* (spread), and (iii) *compatible with a second return* (harmonic check), a weak signature expected when near-recurrences arise by shadowing neighborhoods of unstable periodic orbits.

The only absolute scale entering (5.2) is the hit threshold ε. Rather than fixing ε a priori, we calibrate it from the Pass–1 output using an explicit rule. Let $T_{\text{best}} \in \mathcal{V}$ denote the deepest Pass–1 valley, and fix a target hit-rate level $h_{\min} \in (0,1)$. We set

$$\varepsilon_{\text{need}} := Q_{h_{\min}}\big(\{m_j(T_{\text{best}})\}_{j=1}^{J}\big), \qquad \varepsilon := \max\{\varepsilon_0, \varepsilon_{\text{need}}\},$$

where $m_j(T) = \min_{t \in I_j} \kappa(t)$, $Q_{h_{\min}}$ denotes the $h_{\min}$-quantile, and ε_0 is a baseline scale. The Pass–2 survivor set is then

$$\mathcal{C} := \Big\{T \in \mathcal{V} : \ T \text{ satisfies (5.2)}\Big\},$$

ranked by increasing $\mathcal{S}(T)$, with ties broken by decreasing $h(T,\varepsilon)$ and then increasing stability. Optionally, the top elements of $\mathcal{C}$ may be refined by a local one-dimensional fine scan.

Figure 6 shows the score landscape together with the Pass–1 valleys and the Pass–2 survivors, and Table 1 lists the surviving lags and the local refinement for the leading candidates.

The lag scan on $[T_{\min}, T_{\max}] = [1, 20]$ (with $\Delta T = 0.02$, $J = 20$, $L = 45$, and $\gamma = 0.05$ as specified above) yields a finite candidate set of return-time scales at which the windowed recurrence statistics are simultaneously strong and consistent. In the present dataset, the resulting coarse candidate lags are

$$\mathcal{C}_{\text{coarse}} = \{4.560,\ 5.300,\ 6.880,\ 9.160,\ 12.200,\ 15.220,\ 15.980\},$$

with the associated values of $(\mathcal{S}(T), \mathcal{D}(T), h(T,\varepsilon))$ reported in Table 1. Among these, $T = 9.160$ has the smallest coarse score $\mathcal{S}(T) = 1.578760$, while $T = 5.300$ has the smallest dispersion

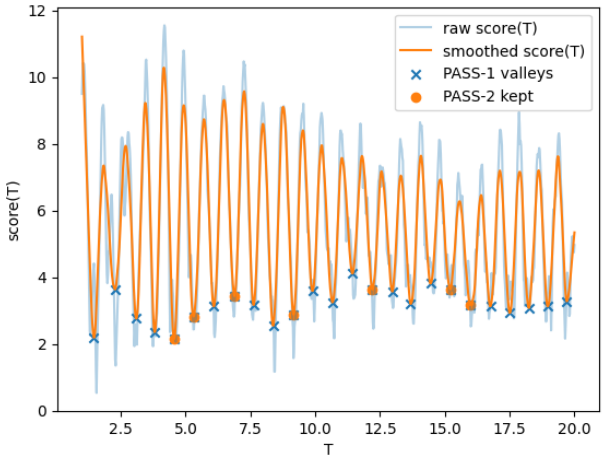

Figure 6. Two-pass lag selection for the Lorenz trajectory on $[T_{\min}, T_{\max}]$. The curve shows the score $T \mapsto \mathcal{S}(T)$. Markers indicate the Pass–1 valley set $\mathcal{V}$ and the Pass–2 survivors $\mathcal{C}$ obtained after enforcing the consistency constraints (5.2).

Table 1. Lag candidates retained by Pass–2 for the Lorenz data. The columns report the coarse-grid values of $\mathcal{S}(T)$, $\mathcal{D}(T)$, and $h(T, \varepsilon)$, and the result of a local fine scan around the corresponding coarse lag.

Rank	T (coarse)	$\mathcal{S}(T)$	$\mathcal{D}(T)$	$h(T, \varepsilon)$	T (refined) / $\mathcal{S}$ (refined)
1	4.560	2.633042	1.126110	0.25	4.605 / 1.943422
2	5.300	2.437875	0.443599	0.45	5.314 / 2.393010
3	9.160	1.578760	2.206991	0.30	9.157 / 1.462177
4	15.980	2.907691	2.426610	0.30	–
5	6.880	2.906431	1.281322	0.25	–
6	12.200	3.271541	2.871118	0.25	–
7	15.220	4.036463	1.658376	0.30	–

$\mathcal{D}(T) = 0.443599$ and the largest coarse hit-rate $h(T, \varepsilon) = 0.45$, indicating comparatively stable and frequent threshold crossings across windows.

To remove grid bias, we refine the three leading candidates by a local one-dimensional fine scan, obtaining

$$\begin{aligned} T &= 4.605, \qquad \mathcal{S}(T) = 1.943422, \\ T &= 5.314, \qquad \mathcal{S}(T) = 2.393010, \\ T &= 9.157, \qquad \mathcal{S}(T) = 1.462177. \end{aligned}$$

For $T = 9.157$, the refined hit-rate increases to 0.55 on the same window family. We therefore select $T^{\star}_{\text{lag}} = 9.157$ for the remainder of the Lorenz analysis, while the other candidates in Table 1 serve as natural alternatives for sensitivity checks.

Section 5.1 provides a *detection* mechanism: It selects time shifts T_{lag} for which the mismatch $\kappa(t, T) = \|x(t+T) - x(t)\|_2$ exhibits statistically significant near-returns along a chaotic

trajectory. These lags are *not* interpreted as periods; they are used only to guide a reproducible event/initialization choice.

The next subsection performs a *local* Poincaré/Newton refinement and produces a periodic-orbit candidate with continuous-time period $T_{\mathrm{po}}^{\star}$, obtained from the accumulated return times. Thus, $T_{\mathrm{po}}^{\star}$ is the period estimate of dynamical interest, whereas $T_{\mathrm{lag}}^{\star}$ is an intermediate detection scale. Any discrepancy between them reflects the transition from global, trajectory-based near-recurrence to a locally refined periodic orbit, rather than two independent period computations.

5.2. From a lag-selected near-return to a refined periodic-orbit candidate

Building on the lag-based event detection in Section 5.1, we use the selected lag $T_{\mathrm{lag}}^{\star} = 9.157$ as a *proposal mechanism* to localize a near-return event along a chaotic trajectory. We then convert this recurrence into a dynamically meaningful periodic-orbit candidate via Poincaré refinement on a transverse section.

Using the same long trajectory as in the lag scan, we record successive crossings of the oriented section $\Sigma = \{x = 0,\ \dot{x} > 0\}$ and denote the section-hit sequence by (t_i, u_i), where $u_i \in \mathbb{R}^2$ are the section coordinates. We choose an index $i^{\star}$ and a return order $p^{\star} \le p_{\max}$ by minimizing a combined criterion that favors (i) a return time close to $T_{\mathrm{lag}}^{\star}$ and (ii) a small mismatch on the section:

$$(i^{\star}, p^{\star}) \in \arg\min_{1 \le p \le p_{\max}} \Big(\big| (t_{i+p} - t_i) - T_{\mathrm{lag}}^{\star} \big| + \lambda \| u_{i+p} - u_i \|_2 \Big), \qquad p_{\max} = 6.$$

For the present dataset, this yields $p^{\star} = 3$ at $i^{\star} = 145$, with

$$t_{i^{\star}+p^{\star}} - t_{i^{\star}} = 9.1648955245, \qquad \| u_{i^{\star}+p^{\star}} - u_{i^{\star}} \|_2 = 3.2794782851 \times 10^{-1}.$$

We take the initial guess $u^{(0)} := u_{i^{\star}} = (1.9685776226,\ 22.4314151492)^{\top}$.

Newton–Poincaré refinement. Starting from $u^{(0)}$, we apply a damped Newton method to the fixed-point problem on the section,

$$F_{p^{\star}}(u) = 0, \qquad F_{p^{\star}}(u) = P^{p^{\star}}(u) - u,$$

where each evaluation of P is performed by event-based numerical integration and the Jacobian $DF_{p^{\star}}$ is approximated by central finite differences. The observed Newton residual decay and the accepted damping factors α_k are reported in Figure 7(b); here α_k is the accepted line-search step length in the update $u^{(k+1)} = u^{(k)} - \alpha_k\, s^{(k)}$.

The refinement produces the fixed-point candidate

$$u^{\star} = (1.9685999513,\ 22.4314662597)^{\top}, \qquad \| F_{p^{\star}}(u^{\star}) \|_2 = 8.2973 \times 10^{-12}.$$

The continuous-time period candidate is obtained by summing the flight times along the $p^{\star}$ successive section returns. Define, for $j = 0, 1, \ldots, p^{\star} - 1$,

$$\tau_j := \tau\big(P^j(u^{\star})\big)\,.$$

Then

$$T_{\mathrm{po}}^{\star} = \sum_{j=0}^{p^{\star}-1} \tau_j = 9.1656785324.$$

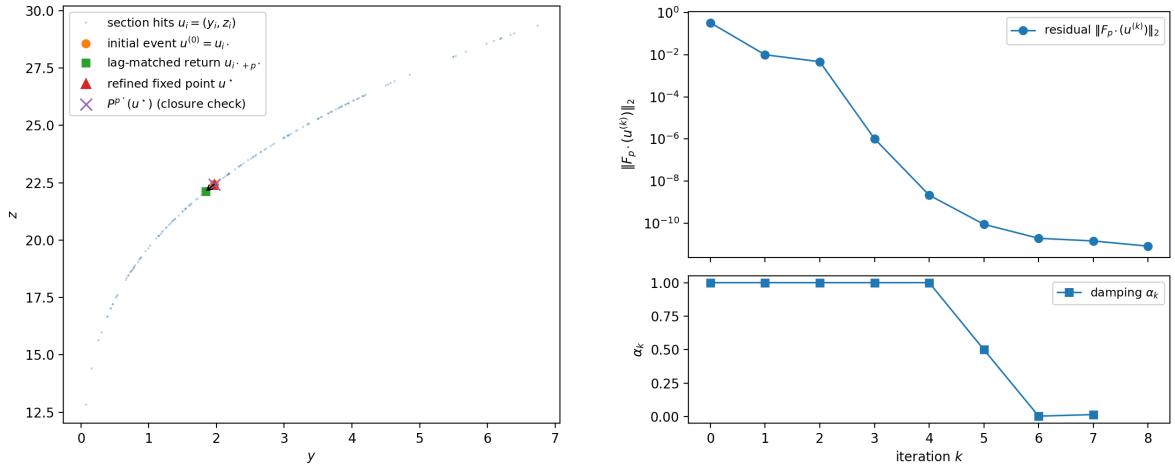

(a) Section data and refinement outcome.

(b) Damped Newton residual and accepted damping.

Figure 7. Lag-driven event selection and Newton–Poincaré refinement on the section Σ. **Left:** Blue dots are section hits $u_i = (y_i, z_i)$; the orange circle is the initial event $u^{(0)} = u_{i^\star}$; the green square is the lag-matched return $u_{i^\star+p^\star}$; the red triangle is the refined fixed point $u^\star$; the purple cross is $P^{p^\star}(u^\star)$ as a closure check. **Right:** Residual $\|F_{p^\star}(u^{(k)})\|_2$ and accepted damping parameters α_k; the α_k series has one fewer element than the residual history because it is defined per accepted step from $u^{(k)}$ to $u^{(k+1)}$.

In the present computation $p^\star = 3$, with individual flight times $\tau_0 = 1.5613991146$, $\tau_1 = 3.0791830620$, and $\tau_2 = 4.5250963558$.

Figure 7(a) visualizes the lag-matched near-return on the section and the refined fixed point $u^\star$, together with the closure check $P^{p^\star}(u^\star)$.

The refinement yields a periodic-orbit candidate $(u^\star, T^\star_{\mathrm{po}})$ whose defect is reduced to the level of numerical integration accuracy. In addition to the section-based residual above, we perform an independent continuous-time closure check by lifting $u^\star$ to $x^\star \in \Sigma$ and evaluating

$$\|\Phi_{T^\star_{\mathrm{po}}}(x^\star) - x^\star\|_2 = 1.1332 \times 10^{-11}.$$

To assess closure along the entire cycle, we plot the phase-dependent mismatch $\kappa_{\mathrm{po}}(t) = \|\Phi_{t+T^\star_{\mathrm{po}}}(x^\star) - \Phi_t(x^\star)\|_2$ over one period in Figure 8, for which

$$\min_{t\in[0,T^\star_{\mathrm{po}}]} \kappa_{\mathrm{po}}(t) = 9.984 \times 10^{-12}, \qquad \max_{t\in[0,T^\star_{\mathrm{po}}]} \kappa_{\mathrm{po}}(t) = 2.409 \times 10^{-7}.$$

Taken together, these diagnostics provide consistent evidence that $(u^\star, T^\star_{\mathrm{po}})$ is a high-accuracy periodic-orbit candidate suitable for subsequent a posteriori validation.

A fully rigorous existence statement for a true solution $u \in \Sigma$ of $F_{p^\star}(u) = 0$ can, in principle, be obtained by verifying the hypotheses of Theorem 3.1 on a neighborhood of $u^\star$. Concretely, such an argument requires computable bounds controlling (i) the defect $\|F_{p^\star}(u^\star)\|$, (ii) the quality of an approximate inverse of $DF_{p^\star}(u^\star)$, and (iii) a validated bound on the variation of $DF_{p^\star}$ in a neighborhood of $u^\star$. In this work we do not claim a verified proof of these bounds. Instead, we report the checkable numerical quantities entering Theorem 3.1 —including the small defect (Figure 7(b)) and the continuous-time closure diagnostics (Figure 8)—and evaluate them at floating-point precision as empirical evidence supporting the refinement and motivating the a posteriori validation step in Section 3.

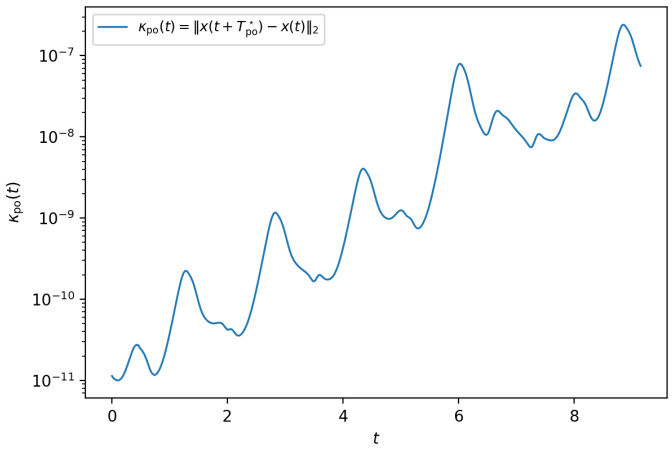

Figure 8. Phase-dependent continuous-time closure defect over one refined period. The curve shows $\kappa_{\mathrm{po}}(t) = \|\Phi_{t+T^\star_{\mathrm{po}}}(x^\star) - \Phi_t(x^\star)\|_2$ for $t \in [0, T^\star_{\mathrm{po}}]$, where $x^\star$ is the lift of $u^\star$ to the section.

5.3. Embedded unstable periodic orbit and intermittent recurrence

We now apply the periodicity-degree framework of Section 2 to the Lorenz double-scroll (5.1) at $(\sigma, \beta, \varrho) = (10, 8/3, 28)$ and interpret the outcome in the chaotic regime. Since the Lorenz vector field is autonomous, the time-T map Φ_T is defined for every $T > 0$ on any bounded region visited by the trajectory segment under consideration; hence the orbitwise mismatch signal $\kappa(t)$ and the associated periodicity indicator $\rho(x(t))$ of Definition 2.2 are well-defined for the lags used below.

Section 5.2 produced, by lag-driven event selection followed by Newton–Poincaré refinement on a transverse section, a refined periodic-orbit candidate $(x^\star, T^\star_{\mathrm{po}})$. In particular, the refinement yields the period estimate

$$T^\star_{\mathrm{po}} = 9.1656785324,$$

together with a continuous-time closure check

$$\|\Phi_{T^\star_{\mathrm{po}}}(x^\star) - x^\star\|_2 = 1.1332 \times 10^{-11}.$$

Figure 9 visualizes this refined candidate in phase space. The segment $x^\star(t)$ over one period lies on the sampled attractor, and the shifted copy $x^\star(t + T^\star_{\mathrm{po}})$ overlays it to plotting resolution. The near coincidence of the marked points $x^\star$ and $\Phi_{T^\star_{\mathrm{po}}}(x^\star)$ is consistent with the above closure defect and supports the interpretation that $(x^\star, T^\star_{\mathrm{po}})$ represents a genuine periodic orbit embedded in the attractor up to numerical accuracy.

A key point is that, in the double-scroll regime, such periodic orbits are typically *unstable*. Consequently, although the orbit exists and is embedded in the attractor, generic trajectories are not periodic and do not converge to it. Instead, they may *shadow* the periodic orbit transiently when they pass near its stable manifold and are subsequently repelled along its unstable directions. This is precisely the regime where the periodicity degree should be interpreted as a *recurrence detector* rather than a global periodicity certificate.

To make this connection explicit, we evaluate the periodicity-degree signal along a generic Lorenz trajectory using the *refined* period $T^\star_{\mathrm{po}}$. Figure 10 shows the resulting time series on the window $[50, 400]$. The signal remains well below 1 for most phases, confirming that the

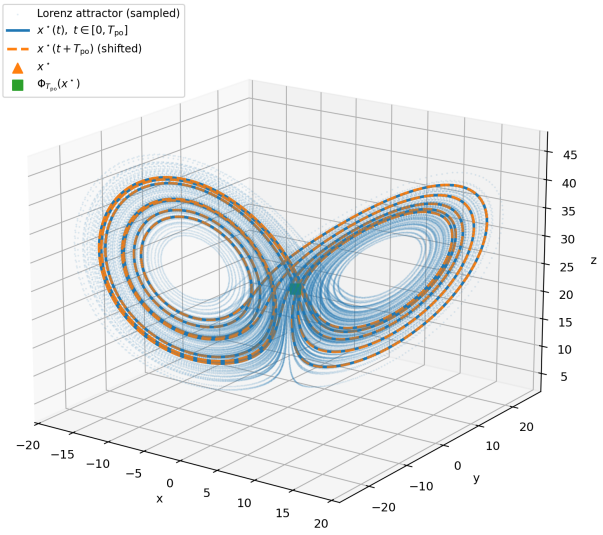

Figure 9. Lorenz attractor together with the refined periodic-orbit candidate $x^\star(t)$ over one refined period $t \in [0, T^\star_{\mathrm{po}}]$ and its time-shifted copy $x^\star(t + T^\star_{\mathrm{po}})$. Markers indicate $x^\star$ and $\Phi_{T^\star_{\mathrm{po}}}(x^\star)$.

trajectory is nonperiodic, but it exhibits intermittent spikes close to 1. These spikes correspond to phases where the one-period mismatch at lag $T^\star_{\mathrm{po}}$ becomes unusually small, i.e. to near-returns after one refined period, which we interpret as transient shadowing events of the embedded periodic orbit. In this sense, the periodicity-degree spikes provide a compact scalar diagnostic that is complementary to recent similarity-signature approaches for characterizing periodic-orbit formation in Lorenz data [14].

The finite-horizon envelopes introduced in Definition 2.2 summarize the strength and variability of these near-returns over the observation window. In the trajectory shown in Figure 10, the computed values are

$$\overline{\rho}_{[50,400]} = 0.9519, \qquad \underline{\rho}_{[50,400]} = 0.0704.$$

The fact that $\overline{\rho}_{[50,400]}$ is close to 1 quantifies the presence of strong recurrent episodes at the refined lag, whereas the small value of $\underline{\rho}_{[50,400]}$ indicates that the same lag can be a poor return time over large portions of the orbit. The pronounced gap between these envelopes is a quantitative signature of phase-dependent recurrence intermittency, which is expected on chaotic attractors containing unstable periodic orbits.

Taken together, Figures 9–10 support the following interpretation: the refined period $T^\star_{\mathrm{po}}$ identifies an unstable periodic orbit embedded in the Lorenz attractor; generic trajectories are nonperiodic but exhibit intermittent near-recurrences at this lag, manifested as spikes of the periodicity degree close to 1. In this chaotic setting, the periodicity degree is therefore most naturally read as a detector of recurrent episodes, while the finite-horizon envelope quantities $\overline{\rho}_{[0,L]}$ and $\underline{\rho}_{[0,L]}$ provide a compact quantitative summary of the strength and variability of such recurrences over the chosen horizon.

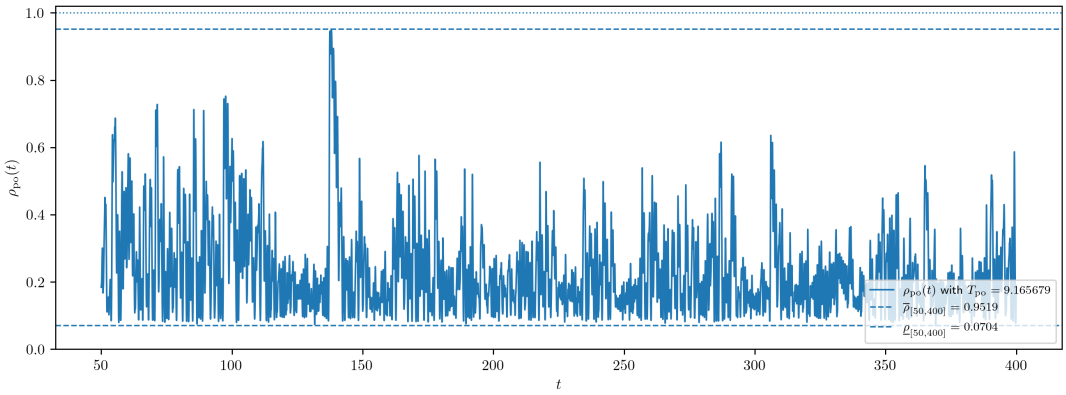

Figure 10. Periodicity-degree signal evaluated at the refined period $T_{\mathrm{po}}^{\star}$ along a generic Lorenz trajectory on $[50, 400]$.

Acknowledgements

The author gratefully acknowledges Professor Yong Li for his guidance and insightful suggestions.

References

[1] D. Auerbach, P. Cvitanović, J. P. Eckmann, et al., *Exploring chaotic motion through periodic orbits*, Physical Review Letters, 1987, 58(23), 2387–2389.

[2] P. Beck, J. P. Parker and T. M. Schneider, *Data-driven guessing and gluing of unstable periodic orbits*, Physical Review E, 2025, 112(2), 024203.

[3] J. B. van den Berg and E. Queirolo, *A general framework for validated continuation of periodic orbits in systems of polynomial ODEs*, Journal of Computational Dynamics, 2021, 8(1), 59–97.

[4] E. A. Coddington and N. Levinson, *Theory of Ordinary Differential Equations*, McGraw-Hill, New York, 1955.

[5] P. Cvitanović, *Periodic orbits as the skeleton of classical and quantum chaos*, Physica D: Nonlinear Phenomena, 1991, 51(1–3), 138–151.

[6] R. Delage and T. Nakata, *Directed recurrence networks for the analysis of nonlinear and complex dynamical systems*, Chaos: An Interdisciplinary Journal of Nonlinear Science, 2025, 35(1), 013107.

[7] E. J. Doedel, H. B. Keller and J. P. Kernévez, *Numerical analysis and control of bifurcation problems (I): Bifurcation in finite dimensions*, International Journal of Bifurcation and Chaos, 1991, 1(3), 493–520.

[8] J. P. Eckmann, S. O. Kamphorst and D. Ruelle, *Recurrence plots of dynamical systems*, Europhysics Letters, 1987, 4(9), 973–977.

[9] M. Engel, O. Ashtari, T. M. Schneider and M. Linkmann, *Search for unstable relative periodic orbits in channel flow using symmetry-reduced dynamic mode decomposition*, Journal of Fluid Mechanics, 2025, 1013, A45.

[10] C. Grebogi, E. Ott and J. A. Yorke, *Unstable periodic orbits and the dimensions of multifractal chaotic attractors*, Physical Review A, 1988, 37(5), 1711–1724.

[11] J. Guckenheimer and P. Holmes, *Nonlinear Oscillations, Dynamical Systems, and Bifurcations of Vector Fields*, Springer, New York, 1983.

[12] A. Hungria, J. P. Lessard and J. D. Mireles James, *Rigorous numerics for analytic solutions of differential equations: The radii polynomial approach*, Mathematics of Computation, 2016, 85(299), 1427–1459.

[13] J. P. Lessard, J. D. Mireles James and J. Ransford, *Automatic differentiation for Fourier series and the radii polynomial approach*, Physica D: Nonlinear Phenomena, 2016, 334, 174–186.

[14] J. Li and Y. Yang, *Similarity signature curves for forming periodic orbits in the Lorenz system*, Chaos, Solitons & Fractals, 2024, 182, 114751.

[15] E. N. Lorenz, *Deterministic nonperiodic flow*, Journal of the Atmospheric Sciences, 1963, 20(2), 130–141.

[16] N. Marwan, M. C. Romano, M. Thiel and J. Kurths, *Recurrence plots for the analysis of complex systems*, Physics Reports, 2007, 438(5–6), 237–329.

[17] E. M. Redfern, A. L. Lazer and D. Lucas, *Dynamically relevant recurrent flows obtained via a nonlinear recurrence function from two-dimensional turbulence*, Physical Review Fluids, 2024, 9, 124401.

[18] G. Teschl, *Ordinary Differential Equations and Dynamical Systems*, American Mathematical Society, Providence, RI, 2012.

[19] W. Tucker, *A rigorous ODE solver and Smale's 14th problem*, Foundations of Computational Mathematics, 2002, 2(1), 53–117.

[20] D. Viswanath, *Symbolic dynamics and periodic orbits of the Lorenz attractor*, Nonlinearity, 2003, 16(3), 1035–1056.

[21] C. L. Webber and J. P. Zbilut, *Dynamical assessment of physiological systems and states using recurrence plot strategies*, Journal of Applied Physiology, 1994, 76(2), 965–973.

[22] J. P. Zbilut and C. L. Webber, *Embeddings and delays as derived from quantification of recurrence plots*, Physics Letters A, 1992, 171(3–4), 199–203.

Received January 2026; Accepted April 2026; Available online April 2026.